CFD Prediction of Aircraft Control Surfaces Aerodynamics

Nunzio Natale[1(✉)], Teresa Salomone[1], Giuliano De Stefano[1], and Antonio Piccolo[2]

[1] Engineering Department, University of Campania Luigi Vanvitelli, 81031 Aversa, Italy
{nunzio.natale,teresa.salomone,giuliano.destefano}@unicampania.it
[2] Leonardo Aircraft Company, 80038 Pomigliano d'Arco, Italy
antonio.piccolo@leonardocompany.com

Abstract. The effectiveness of prototypical control surfaces for a modern regional transport commercial aircraft is examined by means of numerical simulations. The virtual experiments are performed in operational conditions by resolving the mean turbulent flow field around a suitable model of the whole aircraft. The Reynolds-averaged Navier-Stokes modelling approach is used, where the governing equations are solved with a finite volume-based numerical technique. The aerodynamic performance of the flight control surfaces, during an hypothetical conceptual design phase, is evaluated by conducting simulations at different deflections. The present computational modelling approach is verified to have good practical potential by making a comparison with reference industrial data.

Keywords: Computational Fluid Dynamics · Flight control surfaces · Industrial aerodynamics

1 Introduction

Recent progresses in meshing technology, convergence acceleration and calculation performance have allowed Computational Fluid Dynamics (CFD) methods to be intensively used to generate relevant aerodynamic databases, which are particularly useful in the pre-design process of new aircrafts [1,2]. Present trends in industrial aerodynamic design towards cost reduction for product development call for an accurate prediction of the control surfaces aerodynamics, in order to properly arrange the flight control system. The estimation of handling qualities and hinge moments induced by the deflection of the different control surfaces plays a key role in the aircraft sizing process, with a strong impact on the aircraft weight prediction. However, for flows around deployed control surfaces, the complex aerodynamics, as well as the importance of the flight envelope to be covered, makes the numerical simulations particularly challenging.

Differently from typical CFD studies that are performed by employing simplified generic wing-body configurations [3,4], in this study, the computational

© Springer Nature Switzerland AG 2020
O. Gervasi et al. (Eds.): ICCSA 2020, LNCS 12249, pp. 75–89, 2020.
https://doi.org/10.1007/978-3-030-58799-4_6

evaluation of the prototypical configuration of a real regional transport aircraft is performed, with a detailed analysis of the local aerodynamics of the flight control surfaces. The simulations allow to determine the variation of the aerodynamic loads, depending on the deflections of the control surfaces, and thus examine the effectiveness of the control process. Specifically, the effect of ailerons and elevators is studied at a typical flight condition, by means of a number of different calculations. The detailed air flow field is simulated by employing a fully three-dimensional CFD method, while following the Reynolds-averaged Navier-Stokes (RANS) approach. The numerical simulations are conducted using the solver ANSYS Fluent, which is commonly and successfully employed for building virtual wind tunnels in industrial aerodynamics research [5–8]. Indeed, this approach is followed in similar works investigating the aerodynamics of innovative regional aircraft models [9,10]. The feasibility of the proposed computational model for the simulation of complex realistic configurations is assessed through dedicated comparisons with analytical/experimental data provided by the Leonardo Aircraft industrial researchers.

2 Computational Modelling

The preliminary prediction of the global aerodynamic coefficients of interest is obtained using lower fidelity methods, by using either the Vortex Lattice Method (VLM) or a semi-empirical approach [11]. VLM solvers are ideally suited for the preliminary aircraft design environment, where they can be used to predict loads, stability and control data. Some aerodynamic characteristics as lift curve slope, induced drag and lift distribution are obtained through modelling the wing by means of horseshoe vortices distributed along both span and chord, while neglecting the effects of thickness and air viscosity [12].

Furthermore, the aerodynamics of the control surfaces is more accurately predicted by solving the RANS governing equations, which describe the mean turbulent flow field around the aircraft. In this work, the Spalart-Allmaras one-equation model is used, where the turbulence closure is achieved by solving an additional evolution equation for a modified eddy viscosity variable [13]. The turbulent boundary layer is modeled using a wall-function approach. This way, the wall boundary conditions are implemented so that relatively coarser meshes can be used in the calculations. The equations governing the RANS models, which are not reported here for brevity, can be found, for instance, in [14]. The RANS method is commonly used for the simulation of both compressible and incompressible aerodynamic flows, e.g. [15,16].

3 Geometric Models

3.1 Clean Configuration

Isolated Wing. Starting from the computer-aided design (CAD) model of the complete aircraft provided by the Leonardo Aircraft Company, a suitable

Table 1. Clean wings: geometrical data.

Geometrical parameter	Value
Wing area	A
Wing span (without winglets)	b
Wing span (with winglets)	1.03 b
Mean aerodynamic chord, $\overline{c}$	0.086 b
Taper ratio, λ	0.5
Horizontal tailplane area	0.20 A
Horizontal tailplane span	0.28 b
Vertical tailplane area	0.25 A
Vertical tailplane span	0.16 b

geometric sub-model for analysing the isolated wing aerodynamics is initially created. This clean wing model is employed for inviscid calculations conducted to test the in-house methodology that is developed to evaluate the spanwise loading. By removing some features, like nacelles and winglets, the proper comparison with VLM results can be made.

Complete Aircraft. The geometric model for the regional transport aircraft under investigation is comprised of fuselage, wing, empennage, and nacelle groups. Some important geometrical data of the aircraft model are given in Table 1. Here, the different geometrical parameters are expressed in non-dimensional form, by using the wing area A and the wing span b for normalization. The taper ratio λ is defined as the ratio between the tip chord and the root chord of the wing. Note that the actual reference values are not reported in the table, because they are not classified for publication.

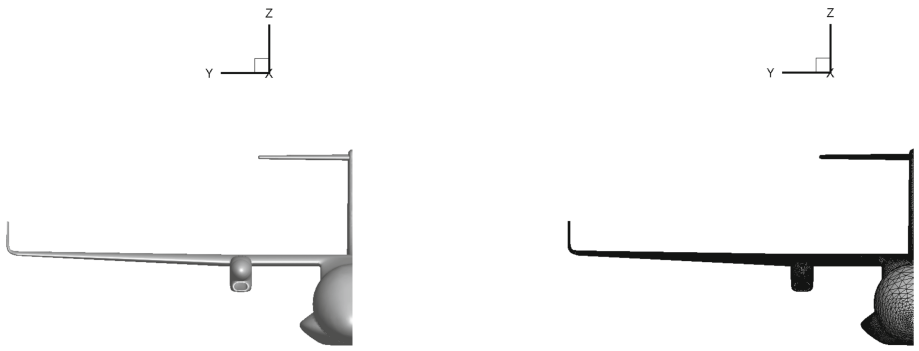

Fig. 1. Clean configuration: frontal views of CAD model (left) and surface mesh (right) for half the aircraft geometry.

A baseline simulation for the clean configuration is first performed. Practically, the gaps between the main aircraft components and the stowed control surfaces are not considered, while the projections of the surfaces edges are maintained, so that the different contributions of the different elements can be evaluated. A hybrid mesh with inflation layers is employed for all the CFD calculations. The numerical simulations for the clean configuration are carried out only for symmetric flow conditions and, thus, half the geometric model is used, while imposing proper symmetry boundary conditions. The FV mesh that is actually used corresponds to the finest mesh produced through a proper sensitivity analysis, being made up of about 7 million elements. Moreover, due to the wall function approach, a suitable first layer thickness is selected, which allows to properly model the boundary layer flow region. The mesh quality, as it holds for all the FV meshes used in this work, can be considered pretty good, especially considering the complexity of the geometrical model. In fact, the maximum skewness of the mesh is less than 0.9 for all the cases, which is within the prescribed limits. The same occurs for other mesh quality parameters, such as the aspect ratio and the orthogonal quality. The frontal view of the aircraft geometry for the clean configuration is presented in Fig. 1, along with the associated surface mesh. Note that the orientation of the reference body axes is such that the x-axis points backward, the y-axis points to the right wing, and the z-axis points upward.

Table 2. Control surfaces: geometrical data.

Geometrical parameter	Value
Aileron starting section, $y_{start}^{\text{aileron}}$	$\pm 0.725\ b/2$
Aileron ending section, y_{end}^{aileron}	$\pm 0.992\ b/2$
Aileron chord ratio, c_a/c	0.3
Elevator starting section, $y_{start}^{\text{elevator}}$	$\pm 0.010\ b/2$
Elevator ending section, $y_{end}^{\text{elevator}}$	$\pm 0.277\ b/2$
Elevator chord ratio, c_e/c	0.33
Horizontal tailplane incidence	i_h
Vertical distance	$z_h - z_w$
Horizontal distance	l_h
Moment calculation reference point	$0.25\ \bar{c}$

3.2 Control Surfaces

The CAD models for the control surfaces are developed by exploiting the geometrical data provided by industrial aerodynamicists. The analysis is conducted by deflecting only one of the control surfaces, while maintaining the others with no

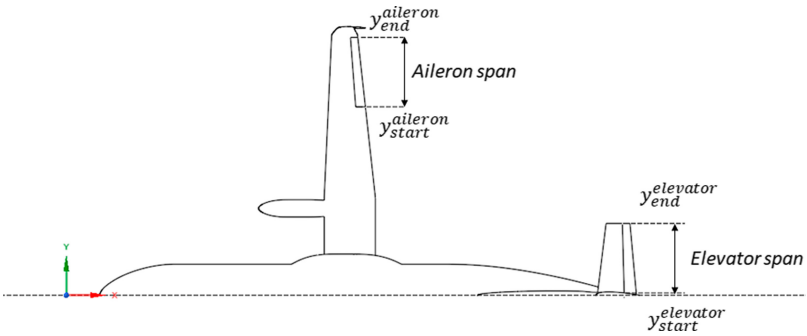

Fig. 2. Control surfaces: geometrical parameters definition.

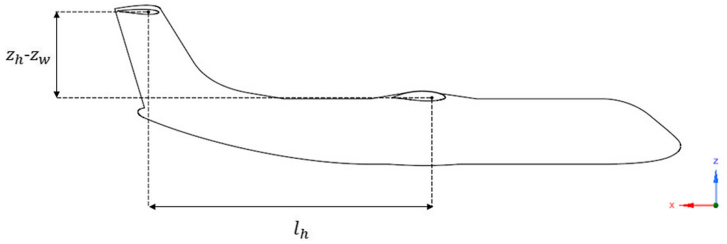

Fig. 3. Aircraft geometry: distances between horizontal tailplane and wing.

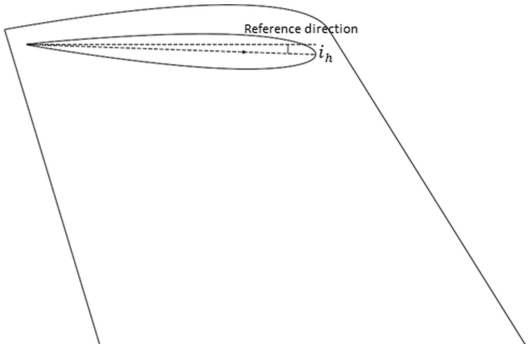

Fig. 4. Horizontal tailplane negative incidence.

deflection. An important aspect to be considered is regarding the gaps between the moving surfaces and the correspondent main components. For each control surface, the upper and lower gaps are closed, while the lateral gaps are kept. Some geometrical data associated to the aircraft control surfaces system are summarized in Table 2, and illustrated in Fig. 2. The characteristic high wing T-tail empennage configuration of the regional transport aircraft under study is illustrated in Fig. 3, where $z_h - z_w$ and l_h represent, respectively, the vertical and

horizontal distances between the horizontal tailplane and the aircraft wing. The incidence of the horizontal tailplane is represented by i_h, which is the negative setting angle of the tailplane chord c_h with respect to the x–axis direction, as depicted in Fig. 4.

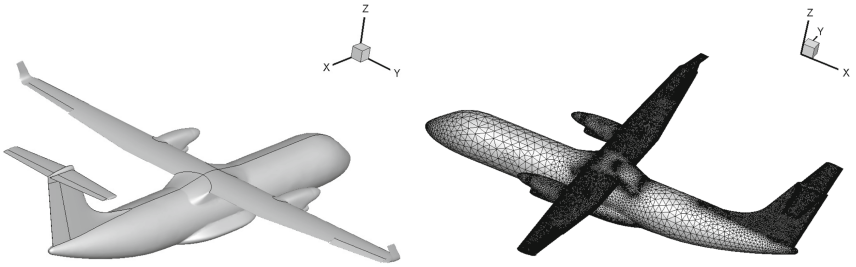

Fig. 5. Ailerons: perspective views of CAD model (left) and surface mesh (right) for the whole aircraft geometry.

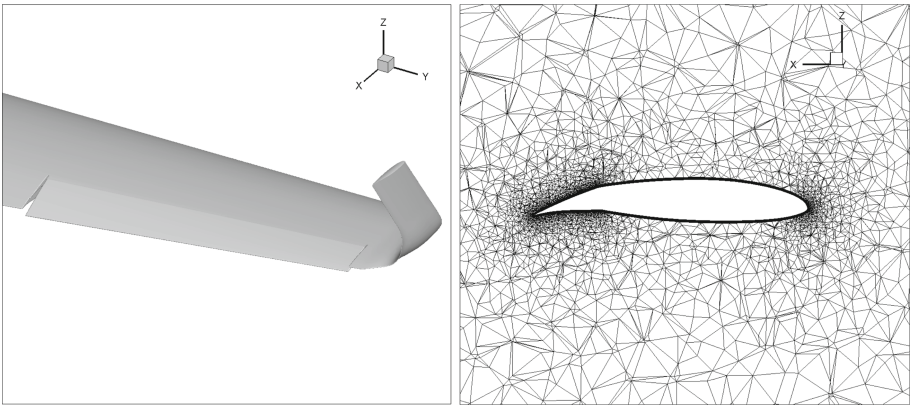

Fig. 6. Right aileron: CAD model (left) and plan view of the volume mesh at the aileron half span section (right).

Ailerons. The CAD model that is developed to study the aerodynamic effect of the ailerons is presented in Figure 5, along with the associated surface mesh. The mesh features are corresponding to those ones considered for the clean configuration, while imposing two opposite deflection angles for the two ailerons, which are $\delta_a = \pm 10°$. Since a symmetrical model can not be employed in this case, the mesh generation is simplified by separately considering the two specular computational sub-domains, while putting a suitable interface between them in

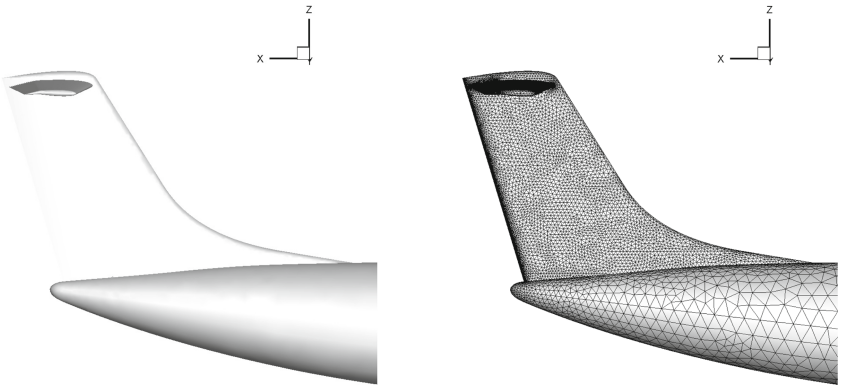

Fig. 7. Right elevator: side views of CAD model (left) and associated surface mesh (right).

the FV mesh used for the calculations. A close-up view of the right aileron is presented on the left side of Fig. 6, while a plan view of the volume mesh corresponding to the aileron half span section is shown on the right side of the same figure. It is worth noting the presence of the inflation layers in the wall region.

Elevators. The model for studying the aerodynamic effect of the elevators is fully consistent with the approach used above. The geometrical characteristics of the elevators are presented in Table 2. In this study, a symmetrical mesh can be used due to the fact that no simulation is performed with non zero sideslip angle. The CAD model for the right elevator is illustrated in Fig. 7, along with the associated surface mesh, for a given positive deflection angle that is $\delta_e = 10°$.

4 Results

The RANS simulations of the mean turbulent flow field around the aircraft model are conducted at Mach number $M_\infty = 0.2$, by employing the Spalart-Allmaras turbulence model, supplied with a wall function approach. The different computational meshes for the different cases are designed to show wall region resolutions that are consistent with the model requirements, as is controlled during the calculations.

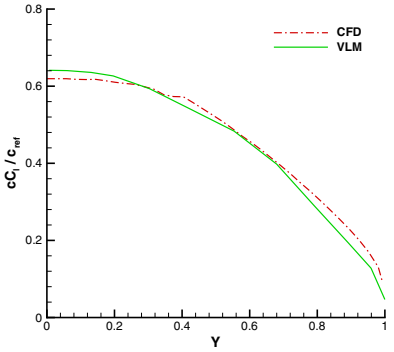

Fig. 8. Isolated wing: spanwise loading distribution for CFD and VLM methods.

4.1 Clean Configuration

Isolated Wing. The loading distribution along the spanwise direction is evaluated through the strip method, by developing a suitable custom field function. Namely, the wing is divided into a series of strips on which pressure and viscous based loads are computed in terms of the product cC_l, where c and C_l stand for the local chord length and the section lift coefficient. As initial verification, the spanwise loading distribution obtained by an inviscid CFD calculation is compared to the VLM-based solution, for a flight condition corresponding to a lift coefficient $C_L = 0.48$. As demonstrated in Fig. 8, where the chord length is normalized by the mean aerodynamic chord ($c_{ref} = \bar{c}$), the agreement between the two different solutions is fully acceptable. In this figure, as well as in the following, the abscissa $Y = y/(b/2)$ represents the normalized coordinate along the spanwise direction.

Complete Aircraft. The model of the complete aircraft in clean configuration is used for a number of numerical tests, whose results are exploited as reference for the following experiments with aerodynamic control surfaces deflected. In the following discussion, the main aerodynamic coefficients and the spanwise loading distributions are examined. In particular, the three different moment coefficients are defined as C_r (rolling), C_m (pitching), and C_n (yawing), where it is assumed $C_r > 0$ when the rolling tends to put the right wing down, $C_m > 0$ when the pitching tends to put the aircraft nose up, and $C_n > 0$ when the yawing tends to put the aircraft nose right. Note that, given the body axes reference introduced above, it practically holds $C_r = -C_{M_x}$, $C_m = C_{M_y}$, and $C_n = -C_{M_z}$, where M_x, M_y and M_z are the moment components along the thee different body-axis directions. The reference point for the moment evaluation is set coincident with the point at one quarter of the mean aerodynamic chord.

A number of steady simulations are conducted at a given flight condition, which is expressed in terms of Mach number and Reynolds number that is $Re_\infty = 11.8 \times 10^6$. The aerodynamic loadings on the aircraft are obtained by

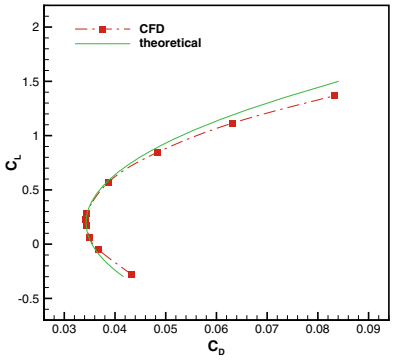

Fig. 9. Clean configuration: drag polar.

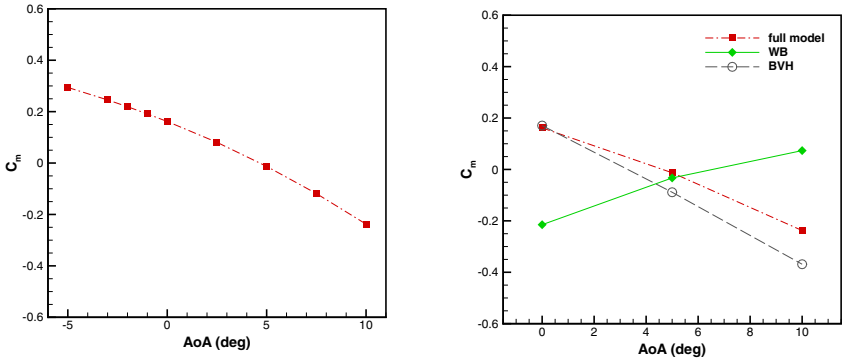

Fig. 10. Clean configuration: pitching moment coefficient (left) and corresponding breakdown (right).

integrating the predicted surfaces forces. The drag polar for the clean configuration is illustrated in Fig. 9, compared with the theoretical parabolic polar, that is

$$C_D = C_{D0} + (C_L - C'_L)^2/(e\pi AR), \tag{1}$$

where C_{D0} stands for the minimum drag coefficient, AR is the aspect ratio and e is the Oswald factor. The present CFD calculations provide C_{D0} equal to 340 drag counts, corresponding to a lift coefficient C'_L of about 0.2. The parabolic curve fitting the numerical data leads to estimate $e = 0.9$ for the Oswald factor. Apparently, the lift coefficient is well predicted for a reasonable operative range of the AoA parameter. The pitching moment coefficient is reported on the left side of Fig. 10, where the negative slope obeys the longitudinal stability criteria. The neutral point has been predicted at 53% of the mean aerodynamic chord, which is consistent with experimental data [17]. The increased C_m slope at high AoA is due to the pendular stability, as is typical for high wing aircrafts [18]. The breakdown of the various contributions to the pitching moment is illustrated

on the right side of Fig. 10. The addition of the vertical tail to the wing-body (WB) combination does not affect C_L and C_m, whereas longitudinal stability is introduced by the horizontal tailplane. The body-tailplanes configuration (BVH) is stable but does not produce useful lift. The complete aircraft configuration has the highest C_L slope due to the additional lift provided by the horizontal tailplane, yet it represents an untrimmed configuration.

4.2 Control Surfaces

In the following, in order to show the capability of the proposed computational modelling, the aerodynamic effect of ailerons and elevators deflection is examined. The results are presented and discussed for some suitable deflection angles.

Ailerons. The aerodynamic effect of the ailerons is presented for deflection angles equal to $\delta_a = \pm 10°$, with the right aileron deflected downward. The predicted spanwise loading distribution is presented in Fig. 11, where the loading is calculated up to the sections immediately before the winglet ($Y = \pm 1$). When making a comparison with the result of the baseline simulation with no deflection, the influence of the ailerons is apparent. In Fig. 12, the rolling moment coefficient variation with the lift coefficient is reported, compared to VLM results. A loss in ailerons effectiveness for $C_L > 0.9$ is observed in the CFD solution, while the VLM method is not able to predict it. The corresponding drag breakdown is illustrated in Fig. 13, where each contribution is expressed in percentage to the total value. Finally, the adverse yaw effect is quantified by the derivative $C_{n\delta_a}$, which is equal to $2.6 \times 10^{-3}\ rad^{-1}$ at zero AoA and rises up to $1.6 \times 10^{-2}\ rad^{-1}$ for an AoA of 7.5°.

Elevators. The aerodynamic effect of the elevators is presented for two different deflection angles that are $\delta_e = \pm 10°$. Figure 14 shows the spanwise loading distribution for the wing and the horizontal tailplane, for both deflections. The presence of the vertical tailplane moves the maximum loading slightly away from the symmetry plane. In particular, the interaction seems to be stronger on the lower surface of the horizontal tailplane. In Fig. 15, the spanwise loading distribution on the horizontal tailplane with elevator deflected, compared with the baseline solution with no deflection, is reported. The corresponding pitching moment coefficient plots are presented on the left side of Fig. 16. Apparently, the horizontal tailplane provides a negative lift when the elevator is not deflected, due to its initial negative incidence with respect to the aircraft centerline ($i_h < 0$) and the downwash effect from the wing. Deflecting the elevator by $-10°$ increases the absolute value of the negative lift. On the other hand, deflecting the elevator by $+10°$ provides a positive lift, that is in absolute value lower than the previous case. The drag polar obtained for $\delta_e = -10°$ is shown on the right side of Fig. 16. It is worth noting that the negative deflection of the elevator leads to a relevant increment of 78 drag counts for C_{D0}. By looking at the drag breakdown, which is reported in Fig. 17, it is interesting to note

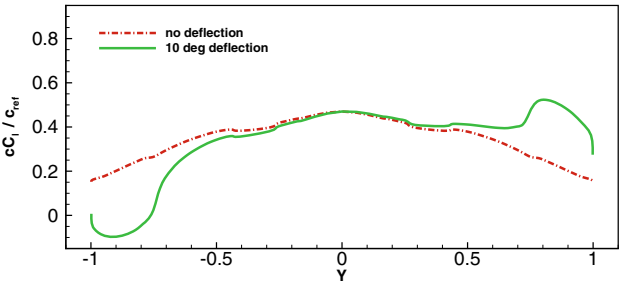

Fig. 11. Ailerons: spanwise wing loading at zero AoA with, and without ailerons deflection.

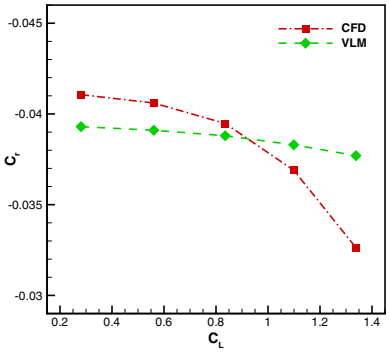

Fig. 12. Ailerons: rolling moment versus lift coefficient.

that deflecting the elevator by $-10°$ (up) leads to higher drag and influences the vertical tailplane as well. This is due to the fact that the elevator leads to higher (negative) load in this case. The pitching moment coefficient variation for the deflection angle $\delta_e = +10°$ is equal to $\Delta C_m = -0.536$, which is comparable to the value obtained using a semi-empirical method that is -0.61 [11]. When making the same analysis for the lift coefficient increment, at zero AoA, it holds $\Delta C_L = 0.109$, while the semi-empirical method providing a value of 0.1. For all the aerodynamic derivatives calculated in the present study, a remarkable matching was found with respect to the values generated by Leonardo Aircraft aerodynamicists. These data were provided as restricted classified data and are not available for public diffusion. Finally, as far as the comparison with the VLM solution is concerned, the discrepancy of the results is large, likely due to differences in the geometries and/or meshes employed. This was also found in similar studies [19].

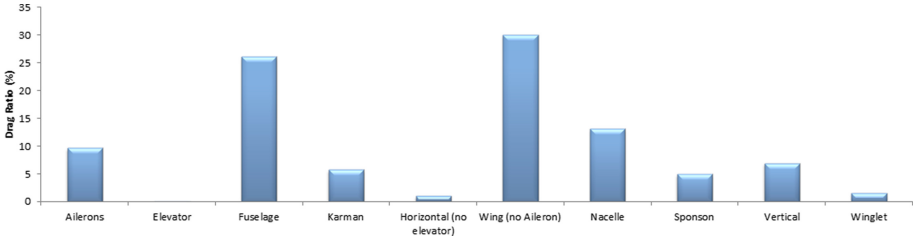

Fig. 13. Ailerons: aircraft drag breakdown.

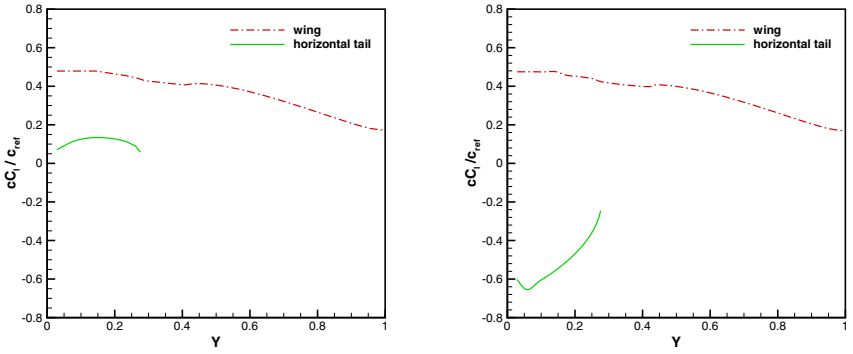

Fig. 14. Elevators: spanwise loading on wing and horizontal tailplane, for $\delta_e = +10°$ (left) and $-10°$ (right).

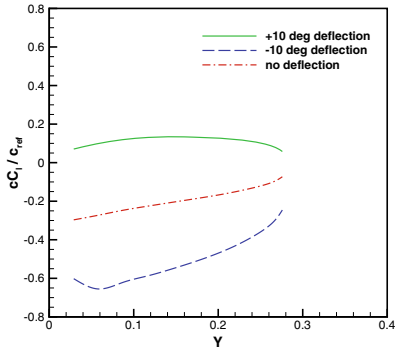

Fig. 15. Elevators: spanwise loading on horizontal tailplane for $\delta_e = +10°$ and $-10°$, compared to clean configuration.

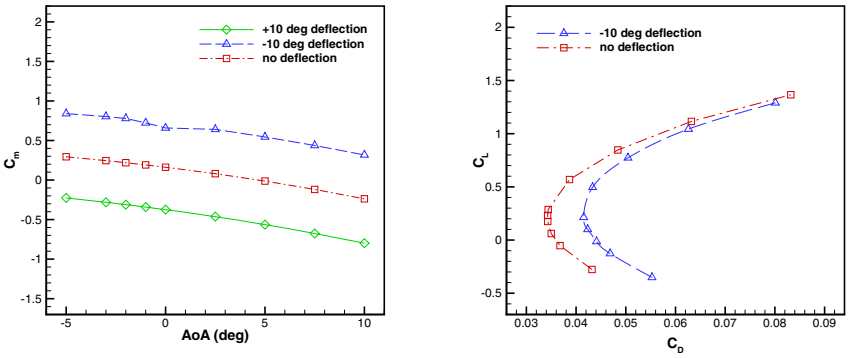

Fig. 16. Elevators: pitching moment coefficient (left) and drag polar (right) for $\delta_e = \pm 10°$, compared to clean configuration.

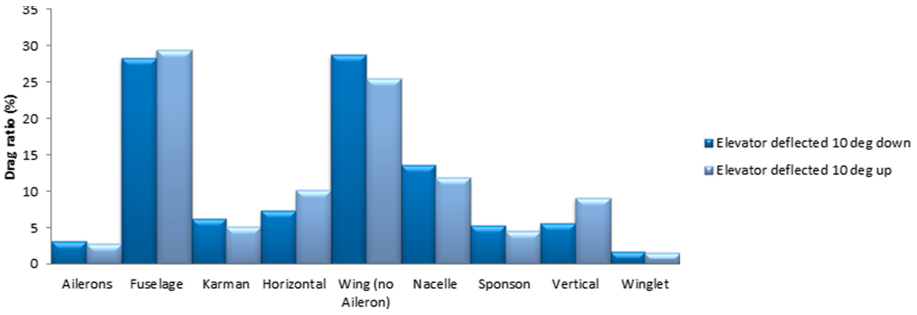

Fig. 17. Elevators: drag breakdown at zero AoA.

5 Conclusions

The present study has to be intended as the proof-of-concept, namely, the preliminary development of a CFD based prediction tool in the aerodynamic design of the control surfaces system of a regional transport aircraft. Differently from similar studies, where the CFD results were obtained for generic geometries, this work deals with simplified models directly derived from real geometries provided by an aeronautical manufacturer that is Leonardo Aircraft Company. Several calculations have been performed with the aim of demonstrating the practical potential of the proposed methodology for the prediction of the control surfaces aerodynamics. The analysis is conducted by performing calculations at a given flight condition and for different deflection angles of ailerons and elevators, while examining the modified aerodynamic force and moment coefficients. It is demonstrated that a complete aerodynamic CFD database can be generated, given the prototypical geometry of the control surfaces, in the pre-design process of new aircrafts. The acceptable agreement with the empirical data made available by the industrial partner has been achieved. There remains the possibility of developing more sophisticated computational models for particular

industrial applications, depending on the level of accuracy that is required and the available computational resources.

Acknowledgements. This work was supported by the Italian Regione Campania under the research project SCAVIR (POR Campania FESR 2014/2020), presented by the Campania Aerospace Technological District (DAC). This support is gratefully acknowledged. The authors would like to thank the Leonardo Aircraft Company for providing the CAD models and the design reference data.

References

1. Johnson, F.T., Tinoco, E.N., Yu, N.J.: Thirty years of development and application of CFD at Boeing Commercial Airplanes. Comput. Fluids **34**, 1115–1151 (2005)
2. Spalart, P.R., Venkatakrishnan, V.: On the role and challenges of CFD in the aerospace industry. Aeronaut. J. **120**(1223), 209–232 (2016)
3. Fillola, G., Le Pape, M.-C., Montagnac, M.: Numerical simulations around wing control surfaces. In: 24th International Congress of the Aeronautical Sciences, Yokohama, Japan, 29 August–3 September 2004 (2004)
4. Mertins, R., Elsholz, E., Barakat, S., Colak, B.: 3D viscous flow analysis on wing-body-aileron-spoiler configurations. Aerosp. Sci. Technol. **9**, 476–484 (2005)
5. Escobar, J.A., Suarez, C.A., Silva, C., López, O.D., Velandia, J.S., Lara, C.A.: Detached-eddy simulation of a wide-body commercial aircraft in high-lift configuration. J. Aircr. **52**(4), 1112–1121 (2015)
6. Reina, G.P., De Stefano, G.: Computational evaluation of wind loads on sun-tracking ground-mounted photovoltaic panel arrays. J. Wind Eng. Ind. Aerodyn. **170**, 283–293 (2017)
7. Rapagnani, D., Buompane, R., Di Leva, A., et al.: A supersonic jet target for the cross section measurement of the 12C(α, γ)16O reaction with the recoil mass separator ERNA. Nucl. Instrum. Methods Phys. Res. B **407**, 217–221 (2017)
8. Benaouali, A., Kachel, S.: Multidisciplinary design optimization of aircraft wing using commercial software integration. Aerosp. Sci. Technol. **92**, 766–776 (2019)
9. Di Marco, A., et al.: Aerodynamic and aeroacoustic investigation of an innovative regional turboprop scaled model: numerical simulations and experiments. CEAS Aeronaut. J. 1–16 (2020)
10. De Stefano, G., Natale, N., Reina, G.P., Piccolo, A.: Computational evaluation of aerodynamic loading on retractable landing-gears. Aerospace **7**(6), 68 (2020)
11. Roskam, J.: Airplane design part VI: preliminary calculation of aerodynamic, thrust and power characteristics. KS, DAR Corporation, Lawrence (2012)
12. Deyoung, J.: Historical evolution of Vortex-Lattice Methods. NASA Langley Res. Center Vortex-Lattice Utilization, 19760021076, pp. 1–9 (1976)
13. Spalart, P.R., Allmaras, S.R.: A one-equation turbulence model for aerodynamic flows. Recherche Aerospatiale **1**, 5–21 (1994)
14. Wilcox, D.C.: Turbulence Modeling for CFD, 3rd edn. DCW Industries Inc., La Canada (2006)
15. Ge, X., Vasilyev, O.V., De Stefano, G., Hussaini, M.Y.: Wavelet-based adaptive unsteady Reynolds-averaged Navier-Stokes simulations of wall-bounded compressible turbulent flows. AIAA J. **58**(4), 1529–1549 (2020)
16. De Stefano, G., Vasilyev, O.V., Brown-Dymkoski, E.: Wavelet-based adaptive unsteady Reynolds-averaged turbulence modelling of external flows. J. Fluid Mech. **837**, 765–787 (2018)

17. Nicolosi, F., Ciliberti, D., Della Vecchia, P., Corcione, S.: Wind tunnel testing of a generic regional turboprop aircraft modular model and development of improved design guidelines. In: AIAA Aviation Forum, Applied Aerodynamics Conference, Atlanta, GA, 25–29 June 2018 (2018)
18. Perkins, C.D., Hage, R.E.: Airplane Performance Stability and Control. Wiley, Hoboken (1949)
19. Mialon, B., Khrabrov, A., Khelil, S.B., et al.: Validation of numerical prediction of dynamic derivatives: the DLR-F12 and the Transcruiser test cases. Prog. Aerosp. Sci. **47**, 674–694 (2011)